Surface & Coatings Technology 347 (2018) 337–349

Contents lists available at ScienceDirect

Surface & Coatings Technology

journal homepage: www.elsevier.com/locate/surfcoat

Surface design of Mg-Zn alloy temporary orthopaedic implants: Tailoring wettability and biodegradability using laser surface melting

Bhaskar Manne[a], Harish Thiruvayapati[a], Srikanth Bontha[a], Ramesh Motagondanahalli Rangarasaiah[a,*], Mitun Das[b], Vamsi Krishna Balla[b]

[a] Department of Mechanical Engineering, National Institute of Technology Karnataka, Surathkal 575025, India
[b] Bioceramics and Coatings Division, CSIR-Central Glass and Ceramic Research Institute, 196 Raja S.C. Mullick Road, Kolkata 700 032, India

ARTICLE INFO

Keywords:
Magnesium alloys
Laser surface melting
Wettability
Biodegradation
Biomineralisation

ABSTRACT

Magnesium-based alloys have attracted significant attention for biomedical applications due to its biodegradability as well as density and elastic modulus which are close to those of human bone. However, the uncontrolled biodegradation and hydrogen evolution are of major concern. In this work, laser surface melting (LSM) has been carried out to tailor initial corrosion rates of Mg-2.2Zn alloy implants. Melt pool dimensions, microstructure and surface topography of the LSM samples were analysed. The wettability and in vitro degradation characteristics of untreated and treated alloy were compared. LSM resulted in much finer cellular microstructural features than as-cast alloy and the melted region depths between 65 and 115 μm. Higher treatment depths helped to extend the corrosion protection time by suppressing the corrosion front movement. Polished LSM samples resulted in overall corrosion rates of 0.5–0.62 mm/year which was about 40%–50% reduction compared to the as-cast alloy. Accelerated biomineralisation of the surface via enhancements in the surface energy due to microstructural refinement as well as microstructural homogeneity and Zn enrichment in α-Mg, favoured improvement of the overall corrosion performance of LSM-treated alloy.

1. Introduction

Magnesium (Mg) alloys have attracted significant attention in the recent past as potential biodegradable orthopaedic and cardiovascular implants [1,2]. Since the Mg-based implants are resorbed by the body, there exist no risks of secondary surgery to remove temporary fracture fixation implants, which is a common practice for bioinert implants made of stainless steel and titanium alloys [3]. Unlike conventional implant materials, Mg reacts with the body fluids and forms non-toxic, soluble reaction products, which are harmlessly excreted through the urine [4–6]. Further, the mechanical properties such as modulus of elasticity, compression strength and density of Mg alloys are very close to those of human bone [7,8]. The similarity in the elastic modulus of Mg alloys to that of the human bone can potentially eliminate or reduce stress shielding and associated failures of bone implants [8]. Several Mg-based binary, ternary and quaternary alloy systems have been studied to understand the mechanical and corrosion properties. In vitro and in vivo studies have been carried out on AZ21 (Al-2 Zn-1) [9], AZ31 [10,11], AZ91 [10,12], WE43 [10,13], WE54 [14], LAE442 [10], ZEK100 [15] and ZM21 [16] alloys which have been originally developed for automotive applications. These alloys contain aluminium (Al) and rare earth elements (RE) which do not contribute to human metabolism and can have adverse effects on human health. For example, the theoretical dose-response assessment conducted by Yuen et al. [17] revealed that the annual exposure limit of Al is 35.88 mg/year for 60 kg adult and no toxicological data is available for RE for present. These low tolerable limits of such alloying elements restrict the overall size of the implants that can be safely implanted. The high tolerable limit of 1122 mg/year for zinc (Zn) [17] increased the interest on Mg-Zn alloys for implant applications. In spite of its low solid solubility (1.6 wt% at room temperature) in Mg, the addition of Zn to Mg promotes both solid solution strengthening and grain refinement leading to their high strength and age hardenability [18,19]. However, the precipitation of Mg_xZn_y intermetallic phase along the grain boundaries of these alloys can promote corrosion [20,21]. It was demonstrated that solution treatment or homogenization treatment can eliminate secondary phases along the grain boundary in Mg-xZn (x = 1–4 wt%) alloys [22] thereby enhancing the corrosion resistance. The passivation of Mg-Zn alloys was found to increase with increasing Zn concentration, but their accelerated hydrogen evolution decreased the overall corrosion performance [22]. The formation of subcutaneous hydrogen bubbles leading to a gap between the implant and the surrounding tissue has been

* Corresponding author.
E-mail address: rameshmr@nitk.edu.in (R. Motagondanahalli Rangarasaiah).

https://doi.org/10.1016/j.surfcoat.2018.05.017
Received 5 January 2018; Received in revised form 9 May 2018; Accepted 10 May 2018

observed in Mg-6Zn alloy implanted in New Zealand rabbit [23]. Therefore, several researchers have attempted to improve or tailor the corrosion properties of Mg-based alloys using a variety of surface treatment techniques such as chemical conversion coatings, plasma arc oxidation, ceramic coatings, shot blasting and laser surface melting (LSM) [24]. Among these techniques, LSM is a simple and fast processing technique that can provide good interfacial characteristics, tailorable thickness, absence of porosity etc. Therefore, LSM has been applied to commercially available automotive grade Mg-Al alloys, AZ31 [25] and AZ91D [26,27] to study its influence on microstructure and corrosion behaviour for biomaterial applications. It has been observed that the LSM results in the enrichment of αMg-phase with Al and fine distribution of β-$Mg_{17}Al_{12}$ secondary phase in the Mg matrix. The high cooling rates associated with LSM resulted in grain refinement thereby improved the corrosion resistance [25–27]. Liu et al., [28] studied LSM of Al8.57%, Zn 0.68%, Mn0.15%, Ce0.52% were investigated using Nd-YAG pulsed laser. They reported improvement in the corrosion resistance due to dendritic grains compared to wrought plate. Laser melting of magnesium alloy powders have also been reported in the literature by the authors Shuai et al. [29] and He et al. [30]. Increasing Zn content up to 4% in Mg-5Sn alloy refined the grains and improved corrosion resistance but corrosion performance degraded with further addition of Zn [29]. Selective laser surface melting (SLM) of AZ61 alloy powders revealed that increased corrosion resistance with increasing power due to increased relative density and uniform grains. Further, increase in power above optimum level resulted in reduced microhardness and corrosion resistance due to evaporation of elements [30]. However, the use of Mg-Al alloys as biodegradable implants is restricted primarily due to the low tolerable limit of the Al and no participation of rare earth elements in the human body [17].

Since, the corrosion of magnesium is partly electrochemical, the corrosion rate (Pi) predicted by the standard electrochemical corrosion techniques is often lower than the actual corrosion rate (Pw) measured using weight loss methods or the corrosion rate (P_H) estimated by the hydrogen evolution method [31]. Song and Atrens [32] reviewed the corrosion mechanism of Mg-based alloys and indicated that the corrosion rates estimated using Tafel extrapolations are inaccurate. Similar inconsistencies in the estimation of corrosion rates using Tafel plots of pure Mg, AZ91 and ZE41 alloys have also been reported [33]. Therefore, for determination of realistic corrosion rate of Mg-based alloys it is suggested to use at least two of the following methods [31]: (i) mass loss (ii) hydrogen evolution and (iii) rate of Mg^{2+} leaving the metal surface (by analysing the Mg concentration in the corrosive solution). Wettability is an important characteristic of biomedical implants which dictates the ion interaction and cell adhesion on the implant's surface. Laser processing is one of the promising technologies for surface texturing and wettability control due to its ability to refine the microstructural features, homogenise the composition and form new or non-equilibrium phases as a result of high cooling rates. LSM found to increase the surface energy of AZ91D alloy from 25.82 to 40.78 mJ/m^2 [34]. Similarly, the wettability of AZ31 alloy has been tailored using pulsed laser surface texturing [35]. Ho et al. [36] demonstrated that the correlation between the roughness, grain size and contact angles or surface energy of AZ31B alloy is highly complex in as-treated condition.

In the present investigation, we have chosen Mg-2.2Zn alloy due to its high tolerable limits in the human body, its positive effect on mechanical and corrosion properties. However, these alloys are known for precipitation of secondary phases which are detrimental to corrosion performance in physiological environment. It is also known that LSM can dissolve such secondary phases in the metal matrix and thus, increases the solubility limits of the alloying elements and refine microstructural features due to characteristic high cooling rates of LSM. Therefore, in this work LSM of Mg-2.2Zn alloy was carried out to understand its effect on the microstructure, compositional changes, surface roughness and in vitro wettability. We also concentrated on long time degradation performance in contrast to works reported by the earlier researchers who focused only on short time electrochemical corrosion performance. An attempt has been made to correlate the degradation rate of LSM Mg-2.2Zn alloy, in Hank's Balanced Salt Solution (HBSS), with microstructural refinement, surface roughness and method of corrosion rate determination.

2. Materials and methods

2.1. Laser surface melting

The Mg-2.2Zn binary alloy (Exclusive Magnesium, Hyderabad, India) cast in a metal mould under CO_2 environment was used. A single plate of 150 × 150 × 5 mm was cut from the ingot and its surface was ground using SiC emery papers followed by ultrasonic cleaning in acetone prior to laser processing. Laser surface melting (LSM) was carried out using Laser Engineered Net Shaping (LENS™) (MR7, Optomec Inc. USA) fitted with continuous wave Ytterbium-doped fibre laser with 0.5 mm beam diameter. The process was carried out in a high purity argon containing glove box using laser powers of 125 W, 175 W and 225 W at scan speeds of 10 mm/s, 20 mm/s and 30 mm/s. An overlap distance of 0.15 mm was used for all samples. Hereafter, the samples were labelled as "power-scan speed" e.g. the samples processed using 125 W laser power and scan speed 10 mm/s were labelled as 125–10.

2.2. Microstructural and phase analysis

The laser-treated samples were sectioned and polished using series of SiC polishing papers (400 to 2000 grit) followed by polishing on velvet cloth using 0.5 μm diamond paste. The polished sections were etched with Picrol reagent to reveal the microstructural features. The microstructures of the base and laser-melted samples were analysed using scanning electron microscopy (SEM, JEOL-JSM-2380LA, Japan). X-Ray diffraction (XRD) analysis was performed using PANalytical X'Pert Pro multipurpose diffractometer with Cu Kα radiation, operating at 30 mA and 40 kV with a step size of 0.05 to determine the changes in the microstructural phases of the Mg-2.2Zn alloy due to LSM.

2.3. Surface topography and wettability

The surface roughness of the LSM-treated samples was determined using Zeta real colour image optical profiler (Zeta-20, Zeta Instruments, San Jose, USA). A field of approximately 1.9 mm × 1.5 mm with 500 steps of size between 0.4 and 0.7 μm were used for the analysis. The data obtained was processed using Zeta software to determine the RMS roughness (Rq) of the samples and an average of ten line roughness measurements was reported for each sample.

The wettability of the as-cast, as-LSM and mechanically polished LSM (abbreviated as PLSM) surfaces was assessed by the sessile drop method. The contact angle measurements were performed using a dynamic contact angle analyser (FTA200, First Ten Angstroms, Inc., Portsmouth, Virginia). A double distilled water drop of approximately 4 μL was dispensed on the surface and the angles were captured continuously. The measurements were carried out at 20 °C. The contact angles were taken considering static equilibrium and an average of five measurements on each sample was reported.

2.4. In vitro degradation studies

For accurate estimation of in vitro degradation/corrosion rates of different sample surfaces, weight loss and hydrogen evolution were monitored and the results were compared. Long-time static immersion corrosion tests were performed on the untreated and laser-processed samples in the cell culture grade Hanks balanced 1× salt solution (HBSS) with pH between 7.4 and 7.6 (Himedia Labs., Bangalore, India). These immersion tests were carried out at room temperature for 72 h by

the immersing Mg alloy samples in 300 mL/cm^2 of HBSS. The samples were exposed to the HBSS on one side (10 × 15 mm) and the other sides were sealed using acrylic resin. In addition, the changes of the solution pH were recorded at regular intervals using a digital pH meter (Systronics, India).

To estimate the corrosion rate by the weight loss method, the samples were first cleaned using a solution prepared with 20 g of CrO_3 added to 80 mL of 0.02 mol/L (0.02 N) $AgNO_3$ followed by cleaning with distilled water to remove the corrosion products from the surface. The cleaned samples were then hot air dried for 15 min and the final weight of the sample was measured using a digital balance with a precision of 0.1 mg. The average corrosion rate of the samples was estimated using the relation:

$$P_w = 3.65\,\Delta W/\rho \quad (1)$$

where, P_w is the average corrosion rate in mm/year, ΔW is the weight loss rate of the sample in mg/cm^2.day and ρ is the density of the alloy (1.768 g/cm^3).

Each mole of Mg (24.306 g) liberates 1 mol (22.4 L) of H_2 during its corrosion. Therefore, the hydrogen evolved during magnesium corrosion provides direct and real time corrosion rates at any instant during the long-term immersion test. In the present investigation the hydrogen evolved during immersion tests was measured using standard inverted funnel and burette arrangement [36]. The precision of the burette used was 0.02 mL. The rate of hydrogen evolved V_H (ml/cm^2.day) can be related to ΔW (mg/cm^2/day) using the following relation [33,37,38]:

$$\Delta W = 1.085\,V_H \quad (2)$$

The corrosion rate in mm/year was calculated by substituting ΔW obtained from Eq. (2) in Eq. (1).

3. Results

3.1. Microstructural analysis

Fig. 1a shows the microstructure of as-cast Mg-2.2Zn alloy consisting of α-Mg grains between 20 μm and 150 μm with Mg_xZn_y secondary phase along the grain boundaries. Fig. 1b–e shows typical cross sections of the LSM-treated Mg-2.2Zn alloy samples. Irrespective of laser process parameters the LSM treatment found to refine the microstructural features such as grain size, Mg_xZn_y precipitate size and distribution. In general, the LSM treated samples exhibited extremely fine microstructures with cellular grains in particular 125–30 samples as shown in Fig. 1c. Relatively coarse microstructures were observed in 225-10 samples (Fig. 1d). The depth of melted region as a function of different laser processing parameters is presented in Fig. 2. The depth of melting increased with increasing laser power and interestingly, also increased with increasing laser scan velocity. For example, the 175-10 combination resulted in 98 ± 3.4 μm while the 175-30 combination resulted in 107 ± 4 μm of melt depth. The largest melt pool depth (110 ± 2.8 μm) was observed in the samples processed at 225 W and 30 mm/s, while lowest depth of 65.4 ± 0.7 μm was recorded in 125-10 sample.

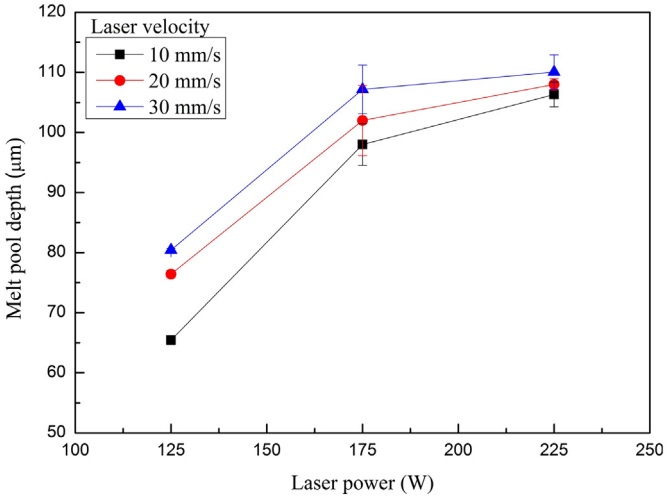

Fig. 2. The influence of laser power and velocity on the melt depth of Mg-2.2Zn alloy.

The compositional analysis in the remelted region was performed using energy dispersive spectroscopy (EDS) to understand the compositional changes. Table 1 provides the summary of typical area composition analysis for the base metal (within the α-Mg grains) and the melted regions of the selected LSM samples. The compositional analysis show that the LSM results in some enrichment and homogenization of Zn within the LM region. Enrichment of the melt pool with Zn content increased with increasing laser energy intensity that can be estimated as the ratio of laser power to beam area. The XRD data of the LSM samples are compared with as cast Mg-2.2An alloy in Fig. 3. Diffraction peak intensities of LSM samples decreased significantly compared to as-cast alloy. The XRD phase analysis confirms the presence of α-Mg phase in the laser melted samples and more importantly peaks corresponding to secondary phase Mg_7Zn_3 were absent as observed in as cast alloy. However, microstructure showed fine and refined secondary particles

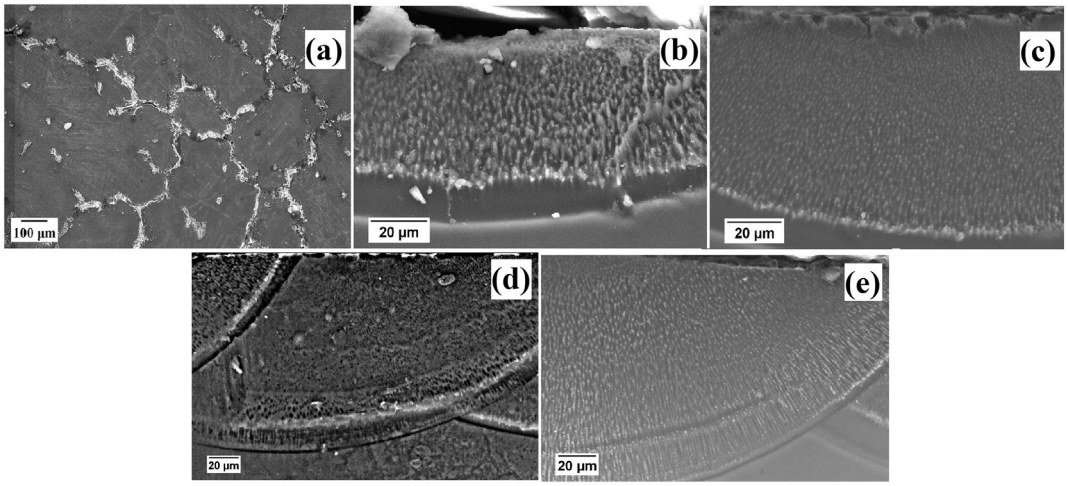

Fig. 1. Typical SEM microstructure of Mg-2.2Zn alloy (a) as received alloy, (b–e) cross sectional microstructures of LSM alloy. (b) 125–10 (c) 125–30 (d) 225–10 (e) 225–30.

Table 1
The EDX compositional analysis (wt%) of as-cast and laser-treated Mg-2.2Zn alloy.

Sample name	Mg	Zn
Base Mg-Zn (within the grains)	97.5 ± 0.8	2.4 ± 0.7
125-30 (lowest energy intensity)	97.3 ± 0.4	2.8 ± 0.4
225-10 (highest energy intensity)	96.4 ± 1.0	3.1 ± 0.7

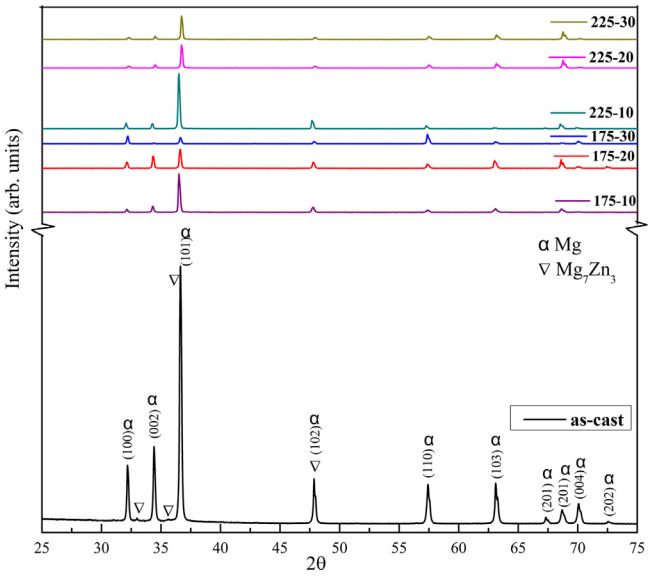

Fig. 3. Comparison of X-ray diffraction patterns of laser melted Mg-2.2 Zn alloy with as-cast alloy.

under low power combination treatments but 225-10 and 225-20 combination did not presence of secondary phases significantly. Diffraction peaks intensity decreased in the samples treated with higher laser velocity while this increased in the samples treated with higher laser power. This corroborates the presence of finest microstructure in 125-30 samples while the coarsest microstructures in 225-10 samples, which corresponds to lowest and highest laser energy intensities, respectively.

3.2. Surface characteristics of laser treated Mg-2.2Zn alloy

The three dimensional (3D) surface profiles of the LSM samples in as-processed condition, presented in Fig. 4a, clearly show characteristic unidirectional tracks representative of LSM tracks on these surfaces. The LSM-treated surfaces revealed track waviness with peaks at the overlapping regions of adjacent laser tracks, some features due to rapid melting followed by solidification, and micro-features such as craters due to the evaporation of surface material during laser surface melting. These surface features can be clearly seen from the line roughness profiles shown in Fig. 4b. The average RMS roughness (Rq) of LSM treated samples is summarized in Table 2. The highest roughness value was observed on 125-30 samples while the lowest roughness values were observed in 175 W power combinations. Since wettability is influenced by the surface topographic features or roughness, the contact angles of distilled water on different Mg-2.2Zn alloy substrates were measured in as-processed and polished conditions (Table 2). Some laser processed alloys such as samples 125-10, 125-20, 225-10 and 225-30 exhibited lower contact angles compared to that of base metal in spite of their high surface roughness. Most of the samples show direct relation with the surface roughness where the contact angles increased with increasing surface roughness. Apart from the average roughness, the surface topography also influences the wettability of a surface. For example, 175 W combination surfaces showed dimple-like structures possibly formed by surface evaporation as evidenced by the high amount of surface inhomogeneity of line roughness profiles shown in Fig. 4b. These inhomogeneities resulted in higher contact angles in 175 W combinations though their overall roughness was lower than other laser treated surfaces. From these results it is difficult to identify the true influence of microstructural changes induced by LSM on the wettability. Therefore, the contact angles were measured on PLSM samples and the results, shown in Table 2, indicate decrease in the contact angles with increasing laser scan speed and an increase with increasing laser power. In order to assess the wettability, the surface energy of polished surfaces was calculated using the measured water contact angles and the following relation [39].

$$E_s = E_{lv} \cos(\theta) \quad (3)$$

where, E_{lv} is the surface energy between water and air (72.8 mJ/m^2 for pure water at 20 °C) and θ is the static wetting angle. The surface energy of different surfaces thus calculated is shown in Fig. 5, showing that the LSM can increase the surface energy of Mg-2.2Zn alloy. Surface energy of the LSM samples increased with increasing laser scan speed and decreased with increasing laser power. Highest surface energy of 51.8 ± 3.7 mJ/m^2 was observed in 125–30 samples due to their finest microstructural features. The lowest surface energy (32.4 ± 4.8 mJ/m^2) was observed in 225–10 combination when compared with the other LM alloys.

3.3. Influence of LSM on in vitro degradation

Figs. 6a–d show the in vitro degradation characteristics of LSM alloy surfaces. The cumulative volume and rate of hydrogen evolution, as determined from the slope of hydrogen evolution versus time curves, are very high in laser-treated samples compared to untreated Mg-2.2Zn alloy substrates (Fig. 7). The evolution of hydrogen continued during the entire duration of immersion and no levelling-off the evolution was observed. The pH changes, shown in Fig. 6b, indicate a rapid increase in the pH of HBSS during the initial period up to 25 h followed by stabilisation of pH between 25 h and 30 h depending on the sample surface. However, the untreated substrate shows stable pH from 17 h onwards of immersion in HBSS as shown in Fig. 7b. Samples with lowest melt region depths (125-10, processed using low energy intensity) suffered highest degradation, while the samples having highest melt region depths (225-30, processed using high energy intensity) exhibited lower corrosion rates. Samples processed at intermediate laser power (175 W) combinations showed lower degradation than other samples. The corrosion rates estimated using hydrogen evolution and mass loss data, Fig. 6c, clearly indicate the strong dependency on surface topography, microstructure refinement and depth of melt region. Therefore, to study the influence of surface roughness on in vitro degradation, the as-cast Mg-2.2Zn alloy substrate was roughened using different SiC emery papers to create varying surface roughness. The corrosion characteristics such as hydrogen evolution, pH change and corrosion rates calculated by mass loss and volume of hydrogen evolved from the as-cast Mg-2.2Zn alloy substrate with different roughness values are presented in Fig. 7a–c. Increase in the hydrogen evolution with time was observed in all samples and lowest cumulative volume and rate of hydrogen evolution were observed in samples with lowest surface roughness (Rq = 2 ± 0.3 μm). The pH of HBSS also increased rapidly up to 15 h of immersion and then stabilized. The corrosion rate was lowest in the Mg-Zn alloy with the lowest surface roughness. From the effects of intentionally created surface roughness on corrosion in as-cast alloy, it is understood that the high corrosion rates in laser-treated alloys could also be due to their high roughness and surface texture formed as a result of melt flow and evaporations during LSM. Accelerated corrosion front from the surface results in faster corrosion of LSM samples.

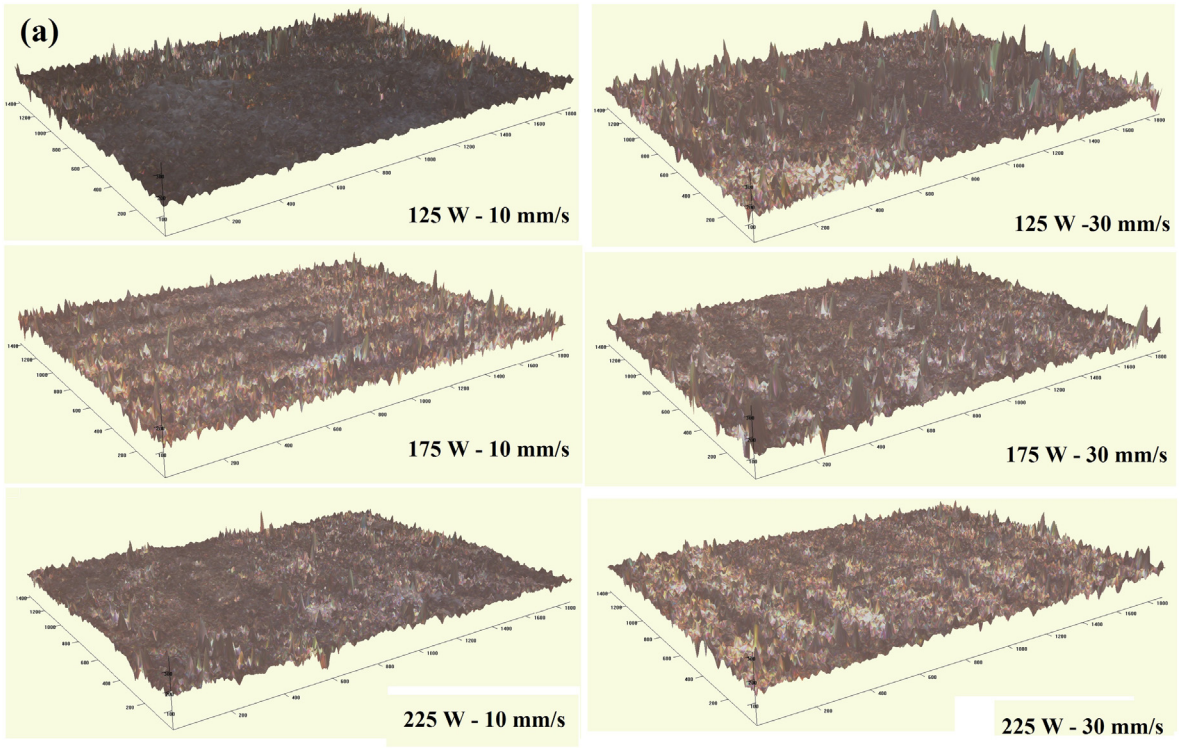

Fig. 4. Typical surface topographies of laser treated Mg-2.2 Zn alloy (a) 3D profiles, (b) roughness profiles in 2D.

Hereafter, the as-cast substrate with lowest roughness (Rq = 2 ± 0.3 μm) were referred to as polished base alloy for comparison with LSM alloy surfaces. Figs. 8a–d show the corrosion characteristics of PLSM samples. After polishing, removing the surface roughness, the hydrogen evolved during in vitro degradation reduced significantly, by almost 50%, in all samples. Similarly, the pH stabilisation occurred early, within 15 h of immersion, in most of these samples compared the same samples in as-laser-treated condition with rough surface. Further, the stabilized pH of HBSS in contact with polished samples was below 8.8 which were significantly lower than that observed with as-laser-treated alloy that revealed pH between 8.8 and 9.5. The corroded samples showed almost a uniform surface degradation (Fig. 8d). The corrosion rate of 225-10 and 225-20 samples were lower than that of the base alloy with approximately same roughness value (Rq = 2) (Fig. 9). Significant variations in the corrosion trends were observed in as-processed and PLSM samples as a function of process parameters. In as-processed condition, the corrosion rates decreased with increasing laser velocity at all power levels while they showed different corrosion rates depending on the surface condition with power variations. Samples having lower melted depths suffered stronger corrosion compared to the samples having higher melt pool depths. Whereas in polished condition, the corrosion rates decreased with increasing laser power at laser scan speeds of 10 mm/s and 20 mm/s, at higher speeds, the corrosion rates did not follow any trend due to the presence of cracks in the melted regions the cross sectional micrographs of which are presented in Fig. 12. However, samples with cracks formed at higher speeds did not show any significant variation in their corrosion rates, where the effect of cracks appeared to have suppressed by the accelerated corrosion front in as-treated samples due to their high roughness.

4. Discussion

Refinement of microstructural features such as the grain size and secondary phases/precipitates can enhance several properties such as mechanical strength, hardness and corrosion resistance etc., of Mg-based alloys. On the one hand, Mg-2.2Zn alloy in cast condition exhibited larger grain size and precipitation of secondary phases along the grain boundaries due to the low cooling rates during conventional casting process. On the other hand, laser surface melting results in significant refinement of microstructural features and the secondary phases. The refinement of these features during laser processing depends on the cooling rates which can be controlled by judicious selection of laser processing parameters. The cooling rate (dT/dt), within the melt pool is generally expressed as the product of thermal gradient (G) and solidification speed (R) [40]. However, the resultant cooling rates also depend on the thermal conductivity of the substrate, physical properties of substrate, laser process parameters and temperature of the substrate. Often the cooling rates experienced by the substrate during laser melting process can be approximately estimated using Rosenthal's equation for a moving point heat source [41]:

$$dT/dt = -2\pi k\left(\frac{V}{Q}\right)\Delta T^2 \quad (4)$$

where, k is thermal conductivity (W/m.K), V is velocity of laser beam, Q is laser power and ΔT is the difference between the liquid metal temperature and the substrate temperature. At the melt pool boundaries, the metal/alloy attains its melting temperature and, assuming the melting temperature and thermal conductivity of Mg-2.2Zn alloy as 922 K and 156 W/m K, respectively, a substrate temperature of 303 K can result in a maximum cooling rate of 9.0×10^4 K/s for 125 W–30 mm/s combination. Similarly, the samples processed at 225 W, 10 mm/s can experience a lowest cooling rate of 1.6×10^4 K/s. Therefore, the highest cooling rates experienced by 125-30 samples resulted in extremely fine microstructural features, while the 225-10 samples showed relatively coarse microstructures due to a reduced cooling rate. From the Eq. (4) it can be inferred that the cooling rate increases with increasing laser scan speed, and increasing laser power decreases the cooling rate which results in coarse microstructural features. The high melt pool temperatures during LSM of Mg-2.2Zn alloy dissolved the secondary phase (Mg_7Zn_3), present in as-cast alloy, and partially suppressed its reprecipitation during solidification due to the rapid cooling rate. The absence of XRD peaks corresponding to this

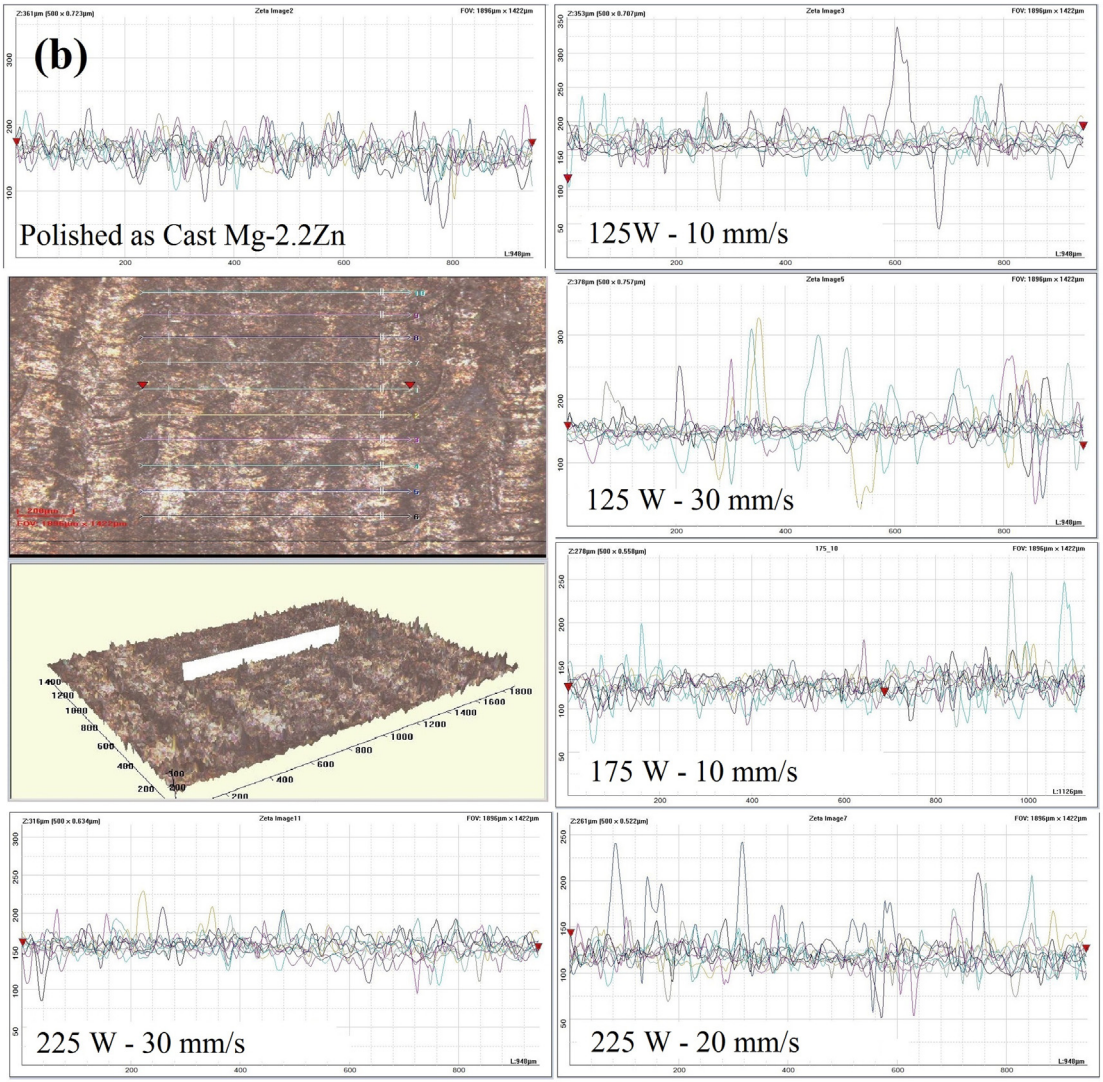

Fig. 4. (*continued*)

Table 2
Average surface roughness (Rq) and double distilled water contact angles (θ) of Mg-2.2 Zn alloy with and without LSM.

Sample	Rq (μm)	θ	
		As-treated	Polished
Base	2.0 ± 0.3	–	66.2 ± 0.4
125-10	13.7 ± 2.2	62.8 ± 4	58.6 ± 1.3
125-20	13.4 ± 1.0	66.1 ± 1.3	49.4 ± 1.5
125-30	21.5 ± 2.6	75.7 ± 4.3	44.6 ± 2.1
175-10	9.7 ± 1.0	71.2 ± 4.3	61.7 ± 1.0
175-20	13.2 ± 1.5	73.8 ± 1.3	51.6 ± 1.3
175-30	11.3 ± 1.2	71.2 ± 3.5	46.8 ± 3.2
225-10	13.1 ± 0.6	63.0 ± 4.0	63.5 ± 2.1
225-20	12.1 ± 0.47	67.7 ± 1.7	56.1 ± 2.3
225-30	11.1 ± 0.4	61.9 ± 2.1	49.2 ± 2.5

secondary phase confirms the existence of rapid cooling rates. Moreover, the presence of a sole α-Mg phase in LSM samples suggests a small increase in the solubility of Zn in Mg as a result of rapid cooling rates experienced by the liquid metal during laser surface melting. The melt pool dimensions depend on total heat input per unit area (I) given as [42]:

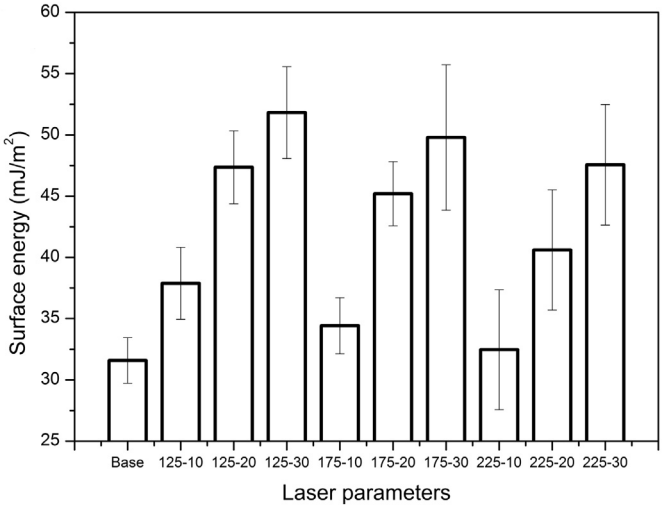

Fig. 5. The influence of laser parameters on the surface energy of polished surfaces of as cast (base) and the PLSM samples.

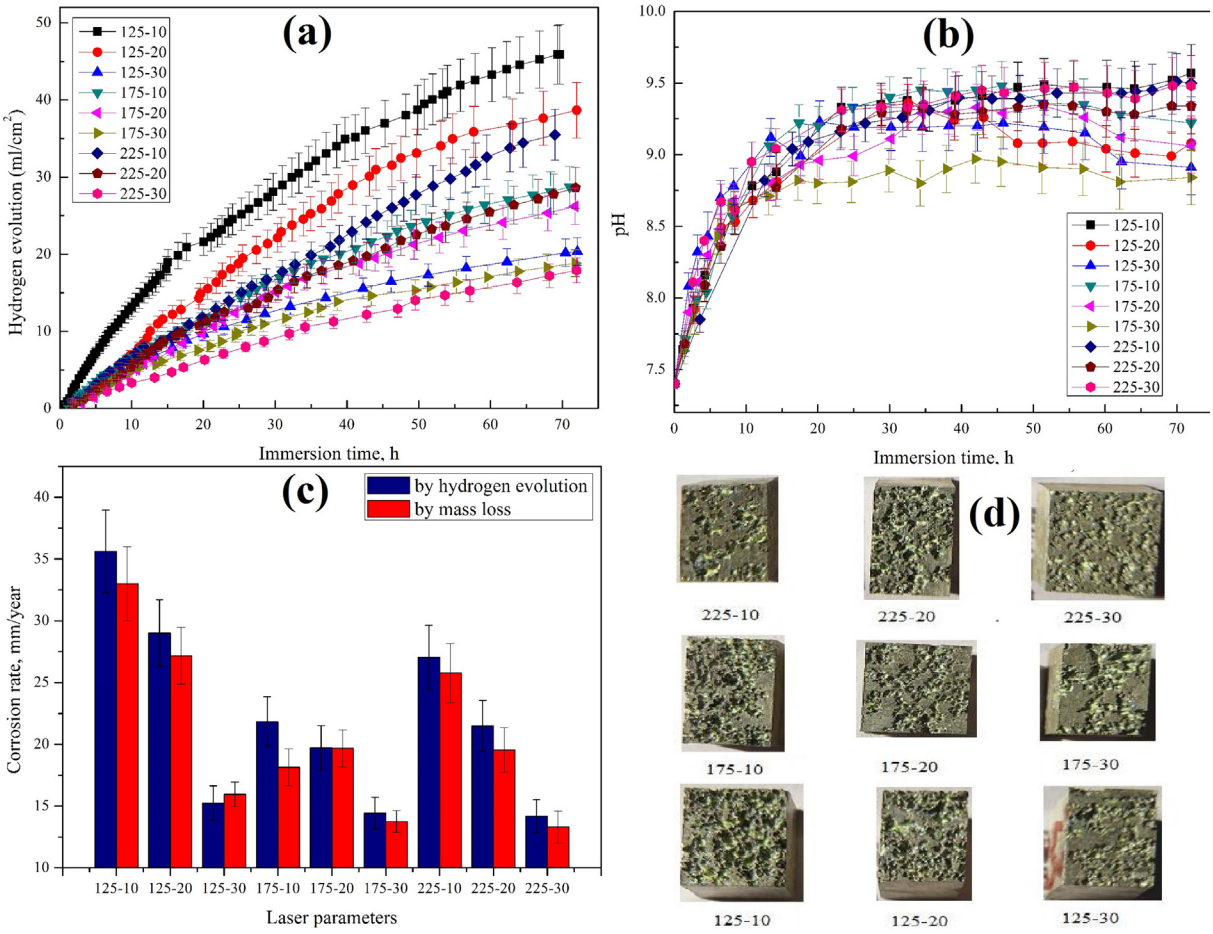

Fig. 6. In vitro degradation of laser treated Mg-2.2Zn alloy in as treated condition (a) Hydrogen evolution (b) pH changes (c) Estimated corrosion rates (d) Images showing the morphologies of corroded Mg-Zn alloy samples after 72 h of immersion in HBSS.

$$I = \frac{Q}{VD} \tag{5}$$

where Q is laser power, V is velocity and D is diameter of the beam. Generally, the melt pool size increases with increasing total heat input. However, our experimental results, Fig. 2, showed decrease in the melt pool depth with increase in velocity, which is contrary to the general trend as per Eq. (5). The observed discrepancies are attributed to the partial evaporation of the top surface of the substrate material as a result of excessive melt pool temperatures generated due to higher resident or incident time of laser beam at the low scan velocities. For example, the resident time of laser beam on the substrate can be approximated as the ratio of beam diameter to scan velocity, which results in resident times of 0.5, 0.25 and 0.16 s for 10 mm/s, 20 mm/s and 30 mm/s scan velocities, respectively. Therefore, we believe that partial evaporation of substrate surface during LSM resulted in decrease in the melt depth of samples with increase in the scan velocity.

The surface texture or topography of an implant is an important factor that controls the wettability and consequently the interactions between the implants and proteins, ions and cells in the physiological environment. It has been observed that the LSM of Mg-2.2Zn alloy results in the variation of surface topographical features and the overall surface roughness increased significantly depending on the laser process parameters used. The formation of different topographical features on LSM samples is primarily due to rapid melting, spreading of the alloy followed by rapid solidification and variations in the amount of shrinkage during solidification of successive overlapping tracks. In particular, surface craters may be caused by evaporation of material from the surface during LSM. The high surface roughness of the samples processed at low laser power, for example 125 W, is believed to be due to uneven contraction due to extremely high cooling rates and insufficient time for spreading of the liquid metal in the overlapping regions of successive laser tracks. With increase in the laser power the cooling rate decreases and hence, the liquid metal has time to spread, leading to suppression of the peaks in the overlap regions. The high surface roughness of samples processed at high incident laser energy is primarily due to partial evaporation of some material from the surface of the substrate due to excessively high melt pool temperatures. The biological activities such as protein adsorption, biomineralisation and cell adhesion on the implant surface have been found to strongly influenced by the wettability of the implant's surface. The surface wettability of a solid is directly related to its surface energy which in turn depends on the surface characteristics such as composition, roughness, grain size, type of phases and their size and distributions. Our experimental results also demonstrated that the surface roughness and topography variations induced by LSM on Mg-2.2Zn alloy had direct influence on distilled water contact angles and consequently the overall surface energy. The lower contact angles of some LSM-treated samples, in spite of their high roughness when compared to untreated alloy, is presumably due to the dominating effects of surface microstructural refinement. Apart from scale of surface roughness and microstructure, the overall topography also influenced the wetting angles. For example, the topography in 175 W combinations due to surface evaporations as evidenced from line profiles (Fig. 4b) resulted in higher contact angles. To eliminate the influence of surface topographic variations among the samples, the contact angles and surface energies of Mg-2.2Zn alloy samples were determined in polished conditions (to ensure identical surface roughness of all sample surfaces). The surface energies

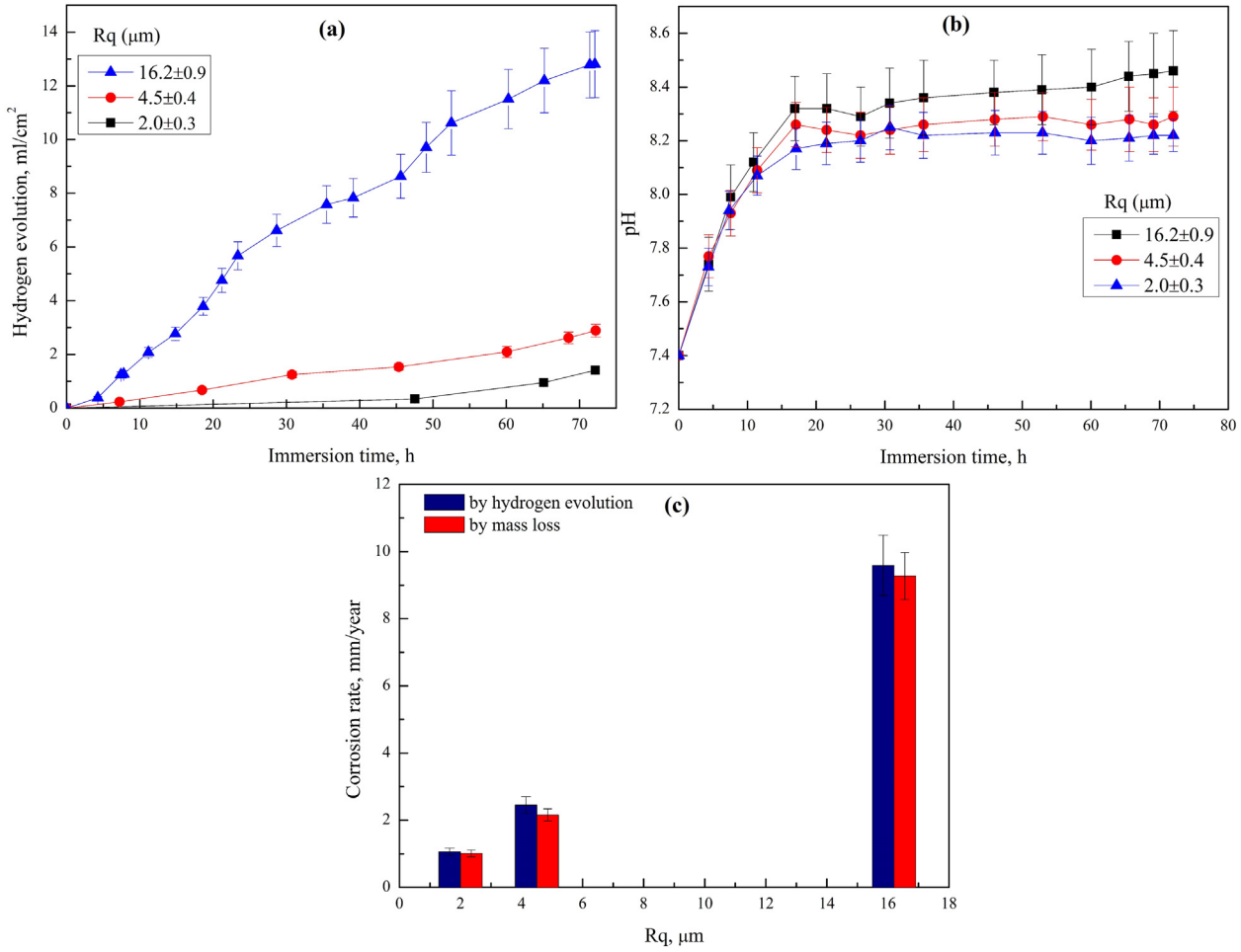

Fig. 7. (a) Hydrogen evolution (b) pH changes (c) Estimated corrosion rates of as cast Mg-Zn alloy as a function of intentionally created surface roughness after 72 h of immersion in HBSS.

calculated from wetting angles of polished samples showed clear correlation with the scale of microstructural features. The experimental results demonstrate that the surface microstructural refinement of LSM-treated alloy samples significantly improve their surface energy compared to the base alloy with coarse microstructural features. The superior wettability of LSM-treated surface may be due to an increased proportion of high-energy grain boundary area as a result of finer grain size. The increase in the surface energy with increasing laser velocity and its decrease with increasing laser power is also directly related to the observed microstructural feature size [43].

The in vivo degradation/corrosion rates of Mg-based implants control the intracellular to extracellular ionic concentration, integration with the natural bone and mechanical stability of the implant during degradation. High rate of degradation results in excessive hydrogen evolution thus leading to a ballooning effect, and an inflammatory reaction in the surrounding tissue. In general, the initial degradation of Mg-based alloys in simulated body fluids results in formation of magnesium hydroxide ($Mg(OH)_2$). Subsequently, the $Mg(OH)_2$ reacts with Cl^- ions present in the solution and forms $MgCl_2$, releasing hydroxyl (OH^-) ions to the solution. This increases the pH of the solution [23], which favours the precipitation of insoluble Mg/Ca-rich phosphate complexes such as $Mg_xCa_y(PO4)_z(OH)$ on implant surfaces [23]. The formation of such biominerals on the surface of the Mg alloy samples minimizes further interaction between the implant and the surrounding environment, and thus stabilizes the pH of the solution. In the present investigation similar observations were recorded on all Mg-2.2Zn alloy samples with and without LSM. The experimental results show that the corrosion rates estimated using hydrogen evolution method were higher than those estimated by mass loss method. The plausible reason for this discrepancy could be due the retention of some residual corrosion products on the sample surfaces during the cleaning step used in mass loss method. However, both corrosion rates, determined using hydrogen evolution and mass loss method, demonstrated strong dependency on the surface characteristics such as topography/roughness, microstructural refinement and melt pool depth (depth of remelted region). In general, the samples with high surface roughness can corrode relatively faster, due to their high surface area to volume ratio, compared to those with low surface roughness. Similar observations were made in the present investigation when the as-cast Mg-2.2Zn alloy with different surface roughness was tested in HBSS (Figs. 7a–c). The LSM-treated alloy samples with surface roughness between 9 and 21 μm exhibited degradation rates between 12 and 35 mm/year. When these laser-treated alloy samples were polished, the corrosion rates decreased by almost 50%, to 0.5 to 15 mm/year, demonstrating the strong influence of surface roughness on in vitro degradation of Mg-2.2Zn alloy. The variations in the corrosion rates of different LSM-treated samples, in as-processed condition, can also be explained based on their LSM-induced surface roughness, depending on the process parameters.

Mg alloy treated by laser in this work showed direct relation with the melt pool depth. LSM-treated samples with lowest melt pool depth showed higher corrosion rates while increase in melt pool depths resulted longer corrosion protection. Generally, the corrosion of laser surface-melted Mg-2.2Zn alloy is believed to occur due to (i) active ion interactions at the crests of tracks, (ii) crevice corrosion due to the

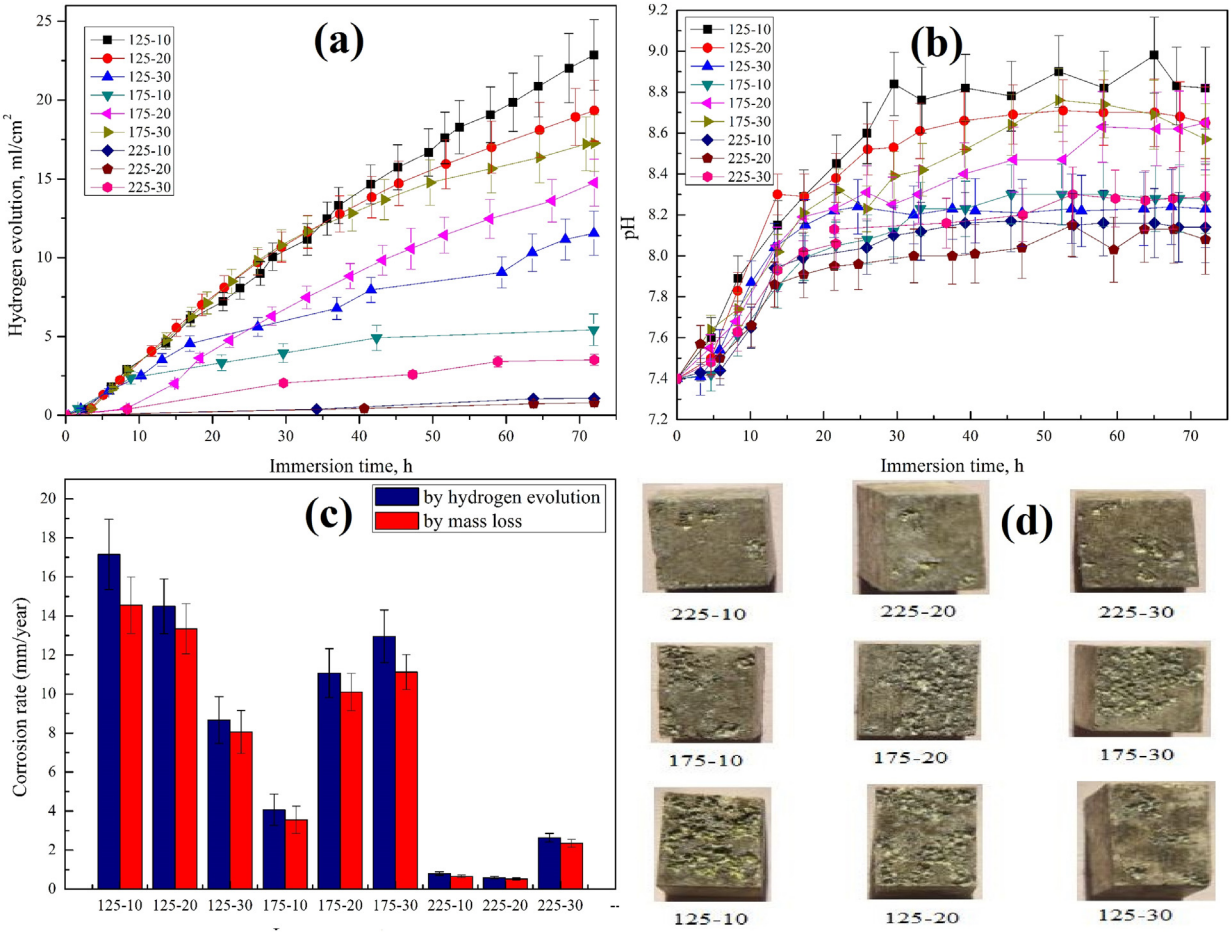

Fig. 8. Degradation of polished surfaces of laser treated Mg-2.2Zn alloy (a) Hydrogen evolution (b) pH changes (c) estimated corrosion rates (d) Morphologies of corroded Mg-Zn alloy samples after 72 h of immersion in HBSS.

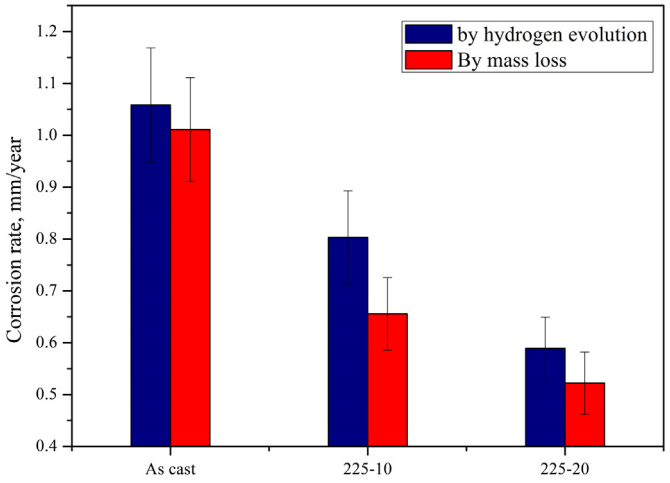

Fig. 9. Comparison of corrosion rates of as-cast (base) and LSM treated Mg-Zn alloy in polished condition after 72 h of immersion in HBSS.

presence of cracks or valleys of surface features and (iii) corrosion due to the formation of galvanic cells between the α-Mg and secondary phases or between the remelted and unmelted regions of the alloy, as shown in Fig. 11a. The general corrosion is initiated at the surface topographic features due to active ionic concentration and can progress further to crevice type corrosion whereby the roughness and solidification cracks at the surfaces can act as anodes and the remaining portion as a cathode. During the process of degradation, when the accelerated corrosion front reaches the bottom of the remelted region, the corrosion front is believed to progress due to (i) the corrosion potential difference between the melt pool, melt pool boundary and the substrate, (ii) differences in internal stresses between the laser-melted region and the substrate, which could initiate stress corrosion. Therefore, the samples with low melt pool depths would have experienced higher degradation due to either of these two phenomena. This is evident from the high rate of hydrogen evolution, 46 mL/cm^2 and pH change of HBSS to 9.5 in 125-10 samples during long time immersion in HBSS.

In LSM, fine and equiaxed grains with or without secondary phases at the grain boundaries and increased solubility of alloying elements found to have positive effects on the corrosion resistance [25–28,30]. However, adequate treatment depth is required to realize such benefits in the long time corrosion tests such as those used in the present work. However, it can be interpreted that the drastic decrease in the corrosion rates of LSM samples, with increase in the laser velocity is due to their finer microstructure. For example, in case of 125-10 samples the corrosion rates were found to be 32.9 ± 3 mm/y while for 125-30, it was found to be 15.9 ± 1 mm/y. These corrosion rates are higher than that of as-cast alloy due to their shallow melt pool depths and balanced positive effect of refined microstructure by negative effect of surface roughness. In case of PLSM samples, the benefits of refined microstructures are again nullified in samples with insufficient melt depths and possible presence of cracks in the melted regions. Second important consideration for the long-term protection of these alloys is the extended solubility of alloying elements in the Mg matrix. These, effects are clearly seen in 225-10 (0.65 ± 0.07 mm/y) and 225-20

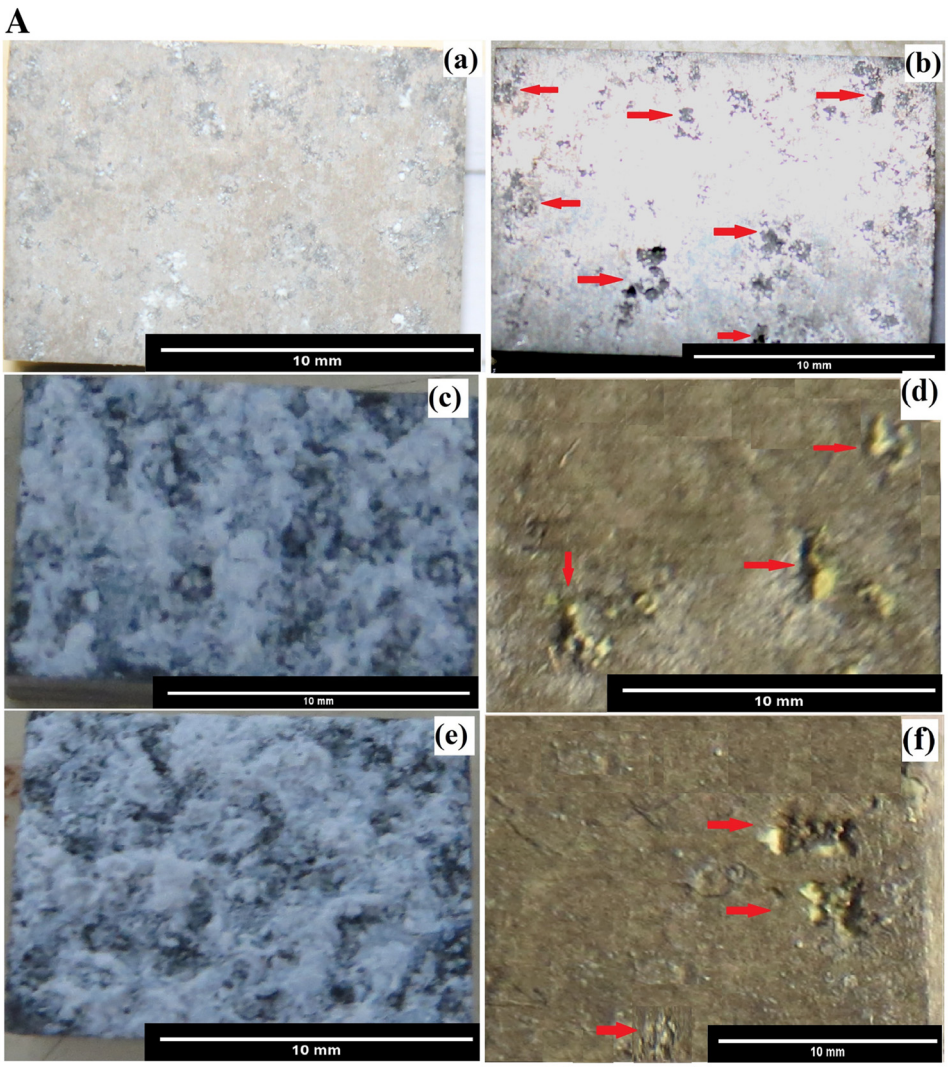

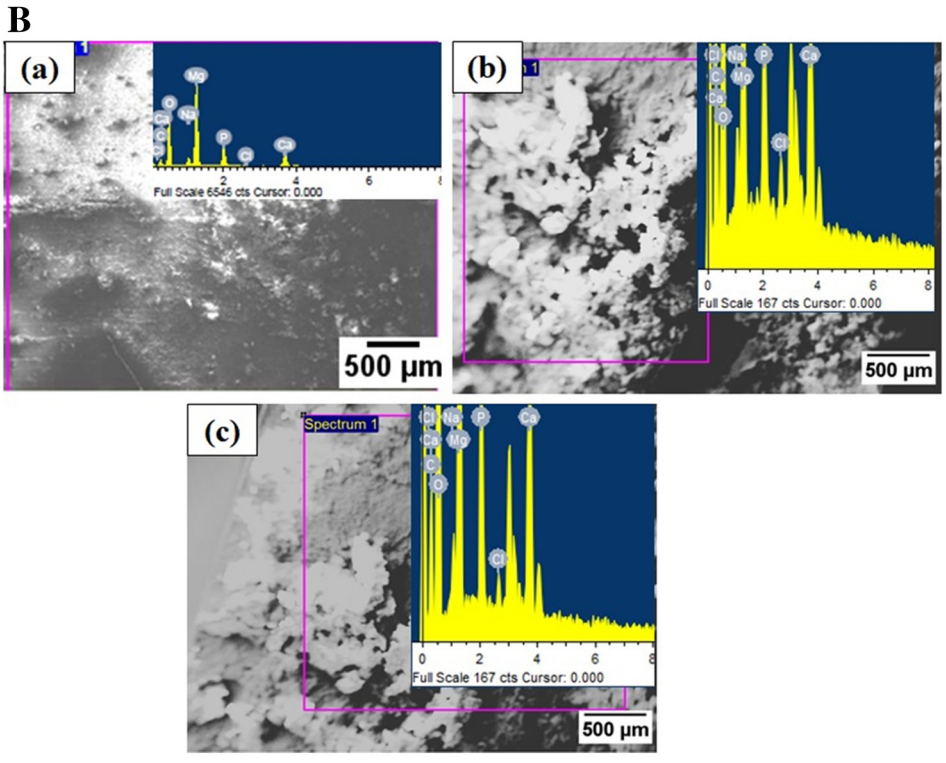

(caption on next page)

Fig. 10. (a) In vitro degraded samples before and after minerals removal for as-cast (a) and (b), PLSM-225-10 (c) and (d) and PLSM-225-20 (e) and (f) respectively. (b) Typical SEM morphologies and EDS analysis of in vitro degraded sarfaces of Mg-Zn alloy immersed for 72 h in HBSS (a) as-cast (b) 225-10, (c) 225-20.

(0.52 ± 0.06) combinations in polished condition where high heat input resulted in Zn enrichment in the melted regions and larger melt pool depths. Zn enrichment in α-Mg increased the resistance to pitting corrosion in these samples whereas the as-cast alloy with no Zn enrichment (1.01 ± 0.1 mm/y) showed lower resistance to pitting corrosion (Fig. 10a).

The decrease in the in vitro degradation of LSM samples after surface polishing as shown in Fig. 8 could be due to the reduction in active ionic concentration on the surface, reduction in the residual stresses (due to mechanical polishing) and removal of any oxidised surface layer (formed during LSM) after polishing. Further, these changes in the surfaces of the LSM samples also decreases the rate of corrosion front movement from the surface towards the substrate and thus delay the corrosion front reaching the boundary between the laser melted region and the substrate. Therefore, the overall degradation rates of the LSM-treated Mg-2.2Zn alloy in the polished condition were lower than those of as-treated alloy samples. Among the laser-treated samples, the corrosion rate decreased with increasing laser power, at scan velocities of 10 mm/s and 20 mm/s, and is due to the increased chemical homogeneity of the remelted region, small enrichment of Zn in the Mg matrix, and high melt pool depths, which resulted in delay of the corrosion front to reach the melt pool boundary. However, the increase in corrosion rate of samples processed at 30 mm/s could be due to solidification cracks, Fig. 12, as a result of high thermal gradients at high scan velocities and their high coefficient of thermal expansion [44]. Interestingly, cracking was found to occur along the grain boundaries of the substrate materials, reaching into the remelted region. This is due to insufficient heat flux required for the formation of sufficient melt pool depth and for reorientation to form new grains needed for crack inhibition. Also, mismatch at the grain boundaries due to high

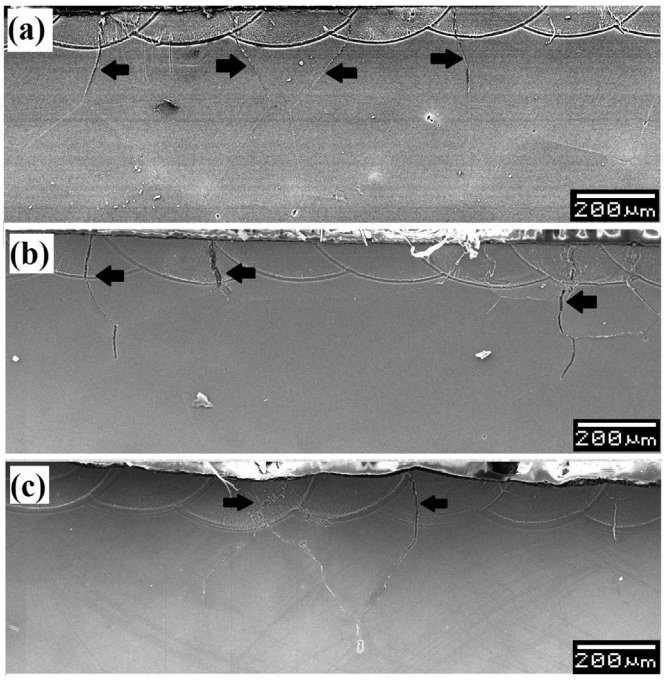

Fig. 12. Cross sectional image showing cracks in LSM samples (a) 125-30, (b) 175-30 and (c) 225-30.

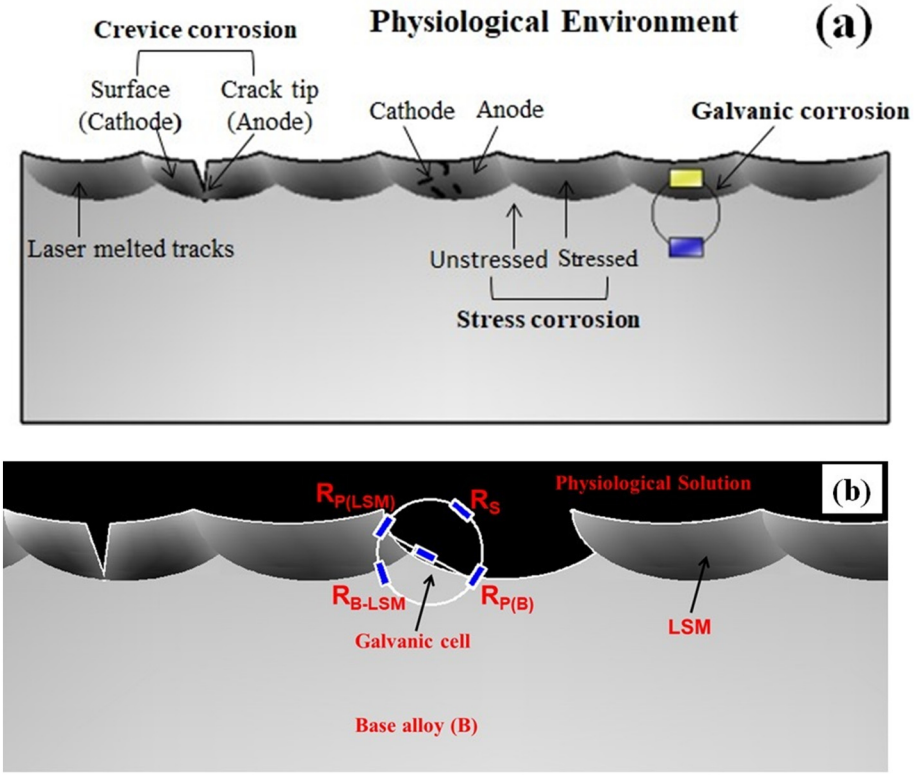

Fig. 11. (a) Schematic diagram showing the general mechanisms of corrosion that can operate on the surface of LSM treated Mg-Zn alloy samples, (b) Electrochemical mechanism believed to operate in the presence of cracks and pits in laser melted samples.

contraction speeds of adjacent grains lead to crack formation. In the past, Guan et al. [34] also reported cracking in the AZ91D Mg alloy due to tensile residual stresses when laser-melted at high laser scan velocities. The electrochemical mechanism that could be operative when the corrosion front encounters any crack or pit is schematically shown in Fig. 11b. The galvanic current (I_g), Eq. 6, due to the pit/crack formation in the laser melted samples can be given as [24]:

$$Ig = \frac{E_{LSM} - E_B}{R_{P(B)} + R_{P(LSM)} + R_s + R_{B-LSM}} \quad (6)$$

where, E_{LSM} and E_B are the corrosion potential of LSM region and base alloy respectively, $R_{P(B)}$ and $R_{P(LSM)}$ are the polarisation resistance of anode (base metal) and cathode (remelted region), respectively. R_S and $R_{B\text{-}LSM}$ are the electrical resistance of solution (HBSS) and electrical resistance between the base metal and the LSM region, respectively.

Among the laser treated Mg-2.2Zn alloy samples, the corrosion rates of 225-10 and 225-20 are lower than that of untreated alloy in the polished condition with similar surface roughness of 2 μm. This is attributed to the combined effects of microstructural refinement, increase in solubility of Zn, as well as sufficient melt pool dimensions to suppress the corrosion front reaching the melt pool boundary through faster biomineralisation. Generally, higher pH values of the body fluids favour the biomineralisation of the surface [23]. However, these LSM-treated samples exhibited excellent biomineralisation, as shown in Fig. 10(a) and (b), in spite of lower pH values of HBSS during immersion study. EDX analysis of the surface confirmed that there is an increase in the Ca and P content on the laser treated surfaces whereas high amount of Mg and Cl were found on the base alloy. Apart from higher pH values the other parameters contributing for enhanced biomineralisation is surface energy. Das et al. [45] reported that increase in the surface energy favours nucleation and growth of hydroxyapatite on the implant surface. Similarly, the increased biomineralisation due to increased surface energy as a result of grain refinement was also reported in friction-stir processed Mg [46] and selective laser melted AZ61 alloy [30].

Our results demonstrate that LSM can be used to tailor the surface properties of Mg-Zn alloy such as wettability, biomineralisation and degradation by corrosion. LSM results in very fine microstructure and microstructural homogeneity as a result of high cooling rates. Thus, improved surface energy due to microstructural refinement, favours accelerated biomineralisation of the surface and thereby improves the bioactivity and decreases degradation rates in physiological environment. Control of treatment depths are easy in LSM by controlling process parameters such as laser power and scan speed. However, sufficiency of melt pool depth, surface roughness and crack free surfaces must be ensured for the effective use of LSM in temporary implants.

5. Conclusion

1. LSM resulted in micron- to submicron-sized cellular microstructures in Mg-2.2Zn alloy. Increasing the laser velocity or decreasing the laser power resulted in finer microstructures. Finest microstructure was observed in the samples treated with 125 W–30 mm/s as a result of high cooling rates during laser melting.

2. Laser treatment resulted in melted region depths in between 65 and 115 μm. The depth of the melt pool increased with increasing laser power and surprisingly also with scan velocity due to surface evaporation. LSM increased the surface roughness of the samples from 9 to 21 μm due to melt flow, evaporation and overlapping adjacent tracks.

3. Roughness and surface texture of the laser-treated samples increased the water contact angles on the surface. In mechanically polished condition, the surface energy estimated from water contact angles increased up to 51 mJ/m^2 with LSM from 29 mJ/m^2 of as-cast alloy. The enhancement in the surface energy is attributed to the microstructural refinement achieved in the alloy surface due to LSM.

4. In vitro degradation of the laser-treated alloy was in Hanks' Balanced Salt Solution (HBSS) at pH between 7.4 and 7.6 much higher due to its high surface roughness. However, for polished samples with Rq = 2 μm the degradation of laser-melted Mg alloy decreased from 1 mm/year of as-cast alloy to 0.65–0.52 mm/year. Improved corrosion resistance is thought to be due to increased microstructural refinement and rapid formation of a protective biomineralized surface layer.

Acknowledgements

The authors would like to acknowledge Dr. Jyoti Ranjan Mohanty, Department of Physics, Indian Institute of Technology Hyderabad, Hyderabad for optical surface profile measurements and Prof. K Narayana Prabhu, Department of Metallurgical and Materials Engineering, National Institute of Technology Karnataka, Surathkal for wettability studies.

References

[1] F. Witte, Reprint of: the history of biodegradable magnesium implants: a review, Acta Biomater. 23 (2015) (S28-S40).
[2] D. Zhao, F. Lu, F. Witte, J. Li, J. Wang, L. Qin, Current status on clinical applications of magnesium-based orthopaedic implants: a review from clinical translational perspective, Biomaterials 112 (2017) 287–302.
[3] F. Witte, The history of biodegradable magnesium implants: a review, Acta Biomater. 6 (2010) 1680–1692.
[4] Merck manual of diagnosis and therapy, water, electrolyte mineral and acid/base metabolism, section 2, Endocrine and Metabolic Disorders, Chapter 12, 1995–2004.
[5] N.-E.L. Saris, E. Mervaalaa, H. Karppanena, K.J.A. Khawajaa, A. Lewenstam, Magnesium: an update on physiological, clinical and analytical aspects, Cln. Chem. Acta. 294 (2000) 1–26.
[6] J. Vormann, Magnesium: nutrition and metabolism, Mol. Asp. Med. 24 (2003) 27–37.
[7] M.P. Staiger, A.M. Pietak, J. Huadmai, G. Dias, Magnesium and its alloys as orthopedic biomaterials: a review, Biomaterials 27 (2006) 1728–1734.
[8] L.-N. Zhang, Z.-T. Hou, X. Ye, Z.-B. Xu, X.-L. Bai, P. Shang, The effect of selected alloying element additions on properties of Mg-based alloy as bioimplants: a literature review, Front. Mater. Sci. 7 (2013) 227–236.
[9] A. Pietak, P. Mahoney, G.J. Dias, M.P. Staiger, Bone-like matrix formation on magnesium and magnesium alloys, J. Mater.Sci. –Mater. Med. 19 (2008) 407–415.
[10] F. Witte, V. Kaese, H. Haferkamp, E. Switzer, A. Meyer-Lindenberg, C.J. Wirth, H. Windhagen, In vivo corrosion of four magnesium alloys and the associated bone response, Biomaterials 26 (2005) 3557–3563.
[11] M. Alvarez-Lopez, M.D. Pereda, J.A. del Valle, M. Fernandez-Lorenzo, M.C. Garcia-Alonso, O.A. Ruano, M.L. Escudero, Corrosion behaviour of AZ31 magnesium alloy with different grain sizes in simulated biological fluids, Acta Biomater. 6 (2010) 1763–1771.
[12] F. Witte, N. Hort, C. Vogtd, S. Cohen, K.U. Kainer, R. Willumeit, F. Feyerabend, Degradable biomaterials based on magnesium corrosion, Curr. Opin. Solid State Mater. Sci. 12 (2008) 63–72.
[13] X.N. Gu, W.R. Zhou, Y.F. Zheng, Y. Cheng, S.C. Wei, S.P. Zhong, T.F. Xi, L.J. Chen, Corrosion fatigue behaviors of two biomedical Mg alloys – AZ91D and WE43 – in simulated body fluid, Acta Biomater. 6 (2010) 4605–4613.
[14] B. Smola, L. Joska, V. Březina, I. Stulíková, F. Hnilica, Microstructure, corrosion resistance and cytocompatibility of Mg–5Y–4Rare Earth–0.5Zr (WE54) alloy, Mater. Sci. Eng. C 32 (2012) 659–664.
[15] D. Dziub, A. Meyer-Lindenberg, J.M. Seitz, H. Waizy, N. Angrisania, J. Reifenrath, Long-term in vivo degradation behaviour and biocompatibility of the magnesium alloy ZEK100 for use as a biodegradable bone implant, Acta Biomater. 9 (2013) 8548–8560.
[16] M. Jamesh, S. Kumar, T.S.N. Sankara Narayanan, Corrosion behavior of commercially pure Mg and ZM21 Mg alloy in Ringer's solution — long term evaluation by EIS, Corros. Sci. 53 (2011) 645–654.
[17] C.K. Yuen, W.Y. Ip, Theoretical risk assessment of magnesium alloys as degradable biomedical implants, Acta Biomater. 6 (2010) 1808–1812.
[18] X. Gu, Y. Zheng, Y. Cheng, S. Zhong, T. Xi, In vitro corrosion and biocompatibility of binary magnesium alloys, Biomaterials 30 (2009) 484–498.
[19] E. Koç, M.B. Kannan, M. Ünal, E. Candan, Influence of zinc on the microstructure, mechanical properties and in vitro corrosion behavior of magnesium–zinc binary alloys, J. Alloys Compd. 648((2015) 291–296.
[20] Y. Song, E.-H. Han, D. Shan, C.D. Yim, B.S. You, The effect of zinc concentration on the corrosion behaviour of Mg-xZn alloys, Corros. Sci. 65((2012) 322–330.
[21] Y. Song, E.-H. Han, D. Shan, C.D. Yim, B.S. You, The role of second phases in the corrosion behaviour of Mg-5Zn alloy, Corros. Sci. 60((2012) 238–245.
[22] H.Y. Ha, J.Y. Kang, J. Yang, C.D. Yim, B.S. You, Limitations in the use of the potentiodynamic polarisation curves to investigate the effect of Zn on the corrosion behaviour of as-extruded Mg–Zn binary alloy, Corros. Sci. 75((2013) 426–433.
[23] S. Zhang, X. Zhang, C. Li, J. Zhao, Y. Song, C. Xie, H. Tao, Y. He, Y. Zhang, Y. Jiang, Y. Bian, Research on an Mg–Zn alloy as a degradable biomaterial, Acta Biomater. 6 (2010) 626–640.
[24] P.K. Chu, G.S. Wu, Surface design of biodegradable magnesium alloys for biomedical applications, in: T.N.S. Narayanan, I.S. Park, M.H. Lee (Eds.), Surface

modification of magnesium and its alloys for biomedical applications: modification and coating techniques, 1 Woodhead Publishing Series in Biomaterials: Number 89, Elsevier, 2015, pp. 101–102.
[25] T.C. Wu, Y.H. Ho, S.S. Joshi, R.S. Rajamure, N.B. Dahotre, Microstructure and corrosion behavior of laser surface-treated AZ31B Mg bio-implant material, Lasers Med. Sci. (2017) 1–7.
[26] Y.C. Guan, W. Zhou, H.Y. Zheng, Effect of laser surface melting on corrosion behaviour of AZ91D Mg alloy in simulated-modified body fluid, J. Appl. Electrochem. 39 (2009) 1457–1464.
[27] C. Taltavull, B. Torres, A.J. Lopez, P. Rodrigo, E. Otero, A. Atrens, J. Rams, Corrosion behaviour of laser surface melted magnesium alloy AZ91D, Mater. & Des. 57((2014) 40–50.
[28] S.Y. Liu, J.D. Hu, Y. Yang, Z.X. Guo, H.Y. Wang, Microstructure analysis of magnesium alloy melted by laser irradiation, Appl. Surf. Sci. 252 (15) (2005) 1723–1731.
[29] C. Shuai, Y. Zhou, X. Lin, Y. Yang, C. Gao, X. Shuai, H. Wu, X. Liu, P. Wu, P. Feng, Preparation and characterization of laser-melted Mg-Sn-Zr alloys for biomedical applications, J. Mater. Sci. Mater. Med. 28 (2017) 13.
[30] C. He, S. Bin, P. Wu, C. Gao, P. Feng, Y. Yang, L. Liu, Y. Zhou, M. Zhao, S. Yang, C. Shuai, Microstructure evolution and biodegradation behavior of laser rapid solidified Mg-Al-Zn alloy, Meta 7 (2017) 105.
[31] A. Atrens, M. Liu, N. Ishide, Z.A. Bidin, Corrosion mechanism applicable to biodegradable magnesium implants—review, Mater. Sci. Eng. B 176 (2011) 1609–1636.
[32] G. Song, A. Atrens, Corrosion mechanisms of magnesium alloys, Adv. Eng. Mater. 1 (1999) 11–33.
[33] Z. Shi, M. Liu, A. Atrens, Measurement of the corrosion rate of magnesium alloys using Tafel extrapolation, Corros. Sci. 52 (2010) 579–588.
[34] Y.C. Guan, W. Zhou, H.Y. Zheng, Effect of Nd:YAG laser melting on surface energy of AZ91D Mg alloy, Surf. Rev. Lett. 16 (2009) 801–806.
[35] A.G. Demir, V. Furlan, N. Lecis, B. Previtali, Laser surface structuring of AZ31 Mg alloy for controlled wettability, Biointerphases 9 (2014) 029009.
[36] Y.-H. Ho, H.D. Vora, N.B. Dahotre, Laser surface modification of AZ31B Mg alloy for bio-wettability, J. Biomater. Appl. 29 (2014) 915–928.
[37] G. Song, A. Atrens, D.St. John, An hydrogen evolution method for the estimation of the corrosion rate of magnesium alloys, in: J.N. Hryn (Ed.), Magnesium Technology 2001 Symposium, Minerals, Metals & Materials Society, New Orleans, LA, 2001, pp. 255–262.
[38] G. Song, A. Atrens, Understanding magnesium corrosion—a framework for improved alloy performance, Adv. Eng.Mater. 5 (2003) 837–858.
[39] R.N. Wenzel, Resistance of solid surfaces to wetting by water, Ind. Eng. Chem. 28 (1936) 988–994.
[40] S. Bontha, N.W. Klingbeil, P.A. Kobryn, H.L. Fraser, Thermal process maps for predicting solidification microstructure in laser fabrication of thin-wall structures, J. Mater. Process. Technol. 178 (2006) 135–142.
[41] W.M. Steen, Laser Material Processing, Springer-Verlag, Germany, 1991.
[42] V.K. Balla, A. Bandyopadhyay, Laser processing of Fe-based bulk amorphous alloy, Surf. Coat. Technol. 205 (2010) 2661–2667.
[43] J.J. Marattukalam, A.K. Singh, S. Datta, M. Das, V.K. Balla, S. Bontha, S.K. Kalpathy, Microstructure and corrosion behavior of laser processed NiTi alloy, Mater. Sci. Eng. C 57((2015) 309–313.
[44] M.M. Avedesian, Magnesium and Magnesium Alloys, ASM International, Materials Park, 1999, pp. 8–9.
[45] K. Das, S. Bose, A. Bandyopadhyay, Surface modifications and cell–materials interactions with anodized Ti, Acta Biomater. 3 (2007) 573–585.
[46] B.R. Sunil, T.S. Kumar, U. Chakkingal, V. Nandakumar, M. Doble, Friction stir processing of magnesium–nanohydroxyapatite composites with controlled in vitro degradation behaviour, Mater. Sci. Eng. C 39 (2014) 315–324.